Science Advances
AAAS

advances.sciencemag.org/cgi/content/full/6/20/eaay0761/DC1

Supplementary Materials for

Direct evidence for efficient ultrafast charge separation in epitaxial WS_2/graphene heterostructures

Sven Aeschlimann*, Antonio Rossi, Mariana Chávez-Cervantes, Razvan Krause, Benito Arnoldi, Benjamin Stadtmüller, Martin Aeschlimann, Stiven Forti, Filippo Fabbri, Camilla Coletti, Isabella Gierz*

*Corresponding author. Email: sven.aeschlimann@gmx.de (S.A.); isabella.gierz@ur.de (I.G.)

Published 13 May 2020, *Sci. Adv.* **6**, eaay0761 (2020)
DOI: 10.1126/sciadv.aay0761

This PDF file includes:

Sections S1 to S5
Figs. S1 to S9

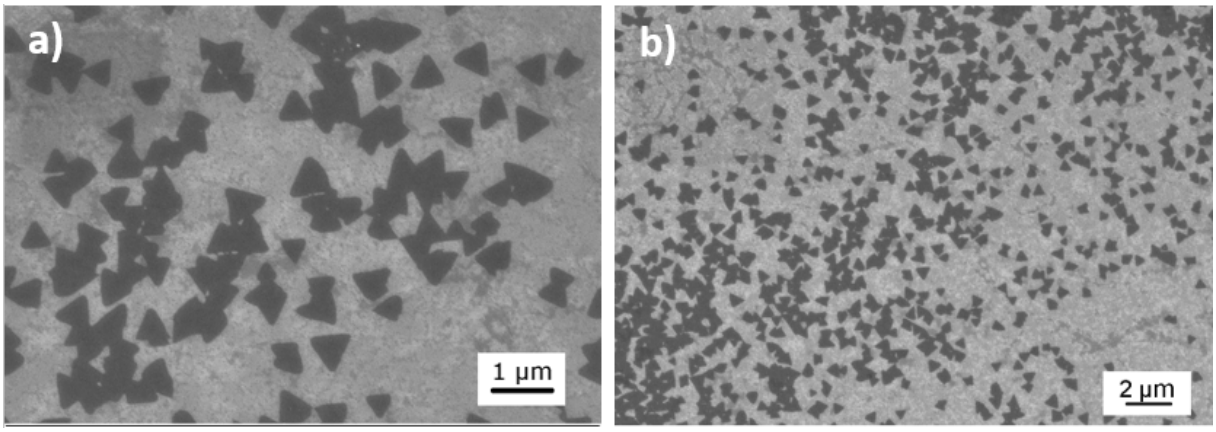

Figure S1: **SEM analysis.** The pictures were obtained with an accelerating voltage of 5 keV and a beam current of 30 pA.

Section S1. Sample Characterization

The WS_2/graphene heterostructures were characterized with secondary electron microscopy (SEM, ZEISS Merlin), atomic force microscopy (Anasys AFM), Raman, and photoluminescence spectroscopy (Renishaw, InVia), as well as low energy electron diffraction (LEED).

SEM (Fig. S1a) reveals WS_2 single-crystalline domains with a side length varying between 300 and 700 nm. In some areas several single crystalline domains are found to merge. From the low magnification image in Fig. S1b we estimate a WS_2 coverage of 40% suitable for the tr-ARPES analysis. The orientation of the WS_2 triangles reveals the presence of two different domains with an angle of 60° between them.

The AFM analysis in Fig. S2 confirms the island size distribution obtained by SEM. In addition, the topographical map reveals that about 10% of the flakes consist of WS_2 bilayers.

The ratio of the 2LA and A1g peak intensities in the Raman spectrum in Fig. S3a confirms the presence of monolayer WS_2 (38). Figure S3b shows the photoluminescence spectrum of the heterostructure with a sharp emission peak at 625 nm (1.98 eV) attributed to the WS_2 A-exciton (39).

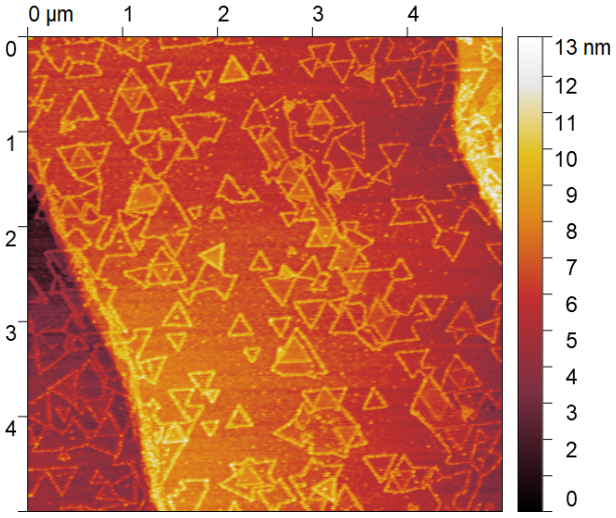

Figure S2: **AFM analysis.**

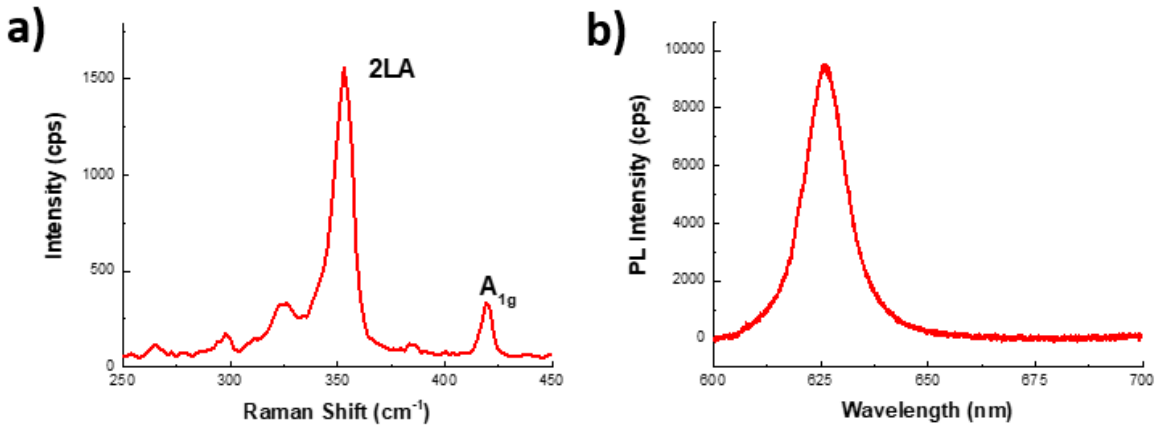

Figure S3: **Raman (a) and photoluminescence spectrum (b).** The measurements were performed with 1 mW 532 nm laser excitation using a 100x-N.A.0.90 objective at room temperature.

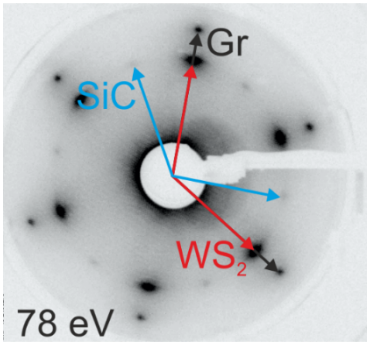

Figure S4: **LEED analysis.** The picture was obtained with an electron energy of 78 eV. Blue, black, and red arrows point to the diffraction spots of the SiC substrate, the graphene layer, and the WS_2 layer, respectively.

In order to assess the crystalline quality of the samples as well as the relative alignment of the WS_2 with respect to the graphene layer LEED measurements were carried out. Prior to the measurement the sample was mildly annealed at 200°C in ultra-high vacuum. The LEED picture in Fig. S4 confirms the perfect azimuthal alignment of the two layers. In combination with the SEM results from Fig. S1 we conclude that the WS_2 islands grow such that either the ΓK- or the ΓK'-direction of the WS_2 island is aligned with the ΓK-direction of the graphene layer.

Section S2. Photo-carrier dynamics of quasi free-standing graphene

In Fig. S5 we present tr-ARPES results for graphene/H-SiC(0001) without WS_2 on top for the same excitation conditions as the ones for the measurements on the WS_2/graphene/H-SiC(0001) heterostructure in the main text. In contrast to the heterostructure (Fig. 2b and c in the main paper) the gain and loss signal for pure graphene in Fig. S5c is symmetric.

Section S3. Tr-ARPES data analysis

We used the following fitting function to extract rise and decay times from the data presented in Figs. 2-4 of the main text:

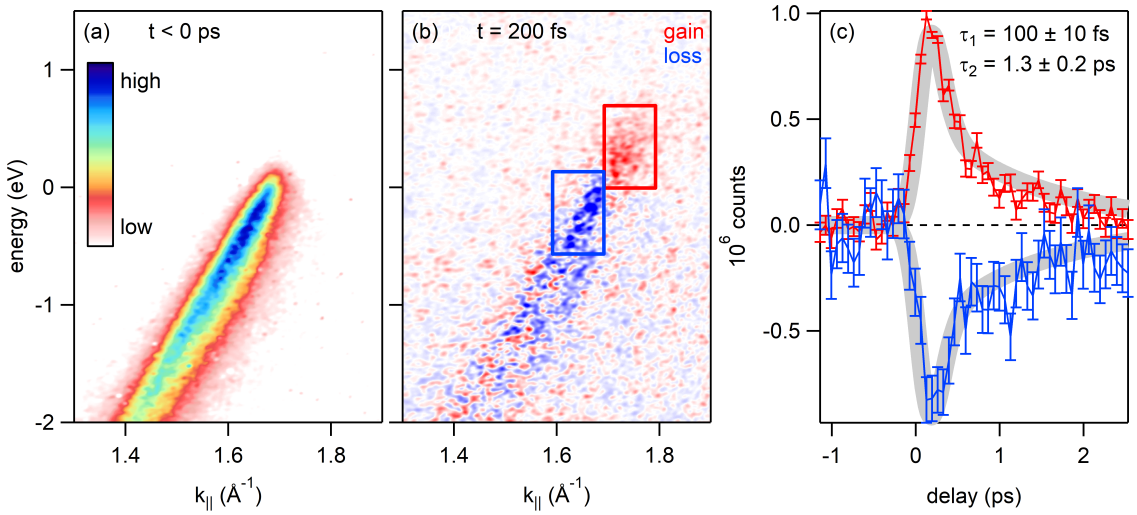

Figure S5: **Photo-carrier dynamics in graphene/H-SiC(0001).** (a) Photocurrent along the ΓK-direction for negative pump-probe delay. (b) Pump-induced changes of the photocurrent 200 fs after photo-excitation at a pump photon energy of 2 eV with a pump fluence of 2 mJ/cm^2. Gain and loss of photoelectrons are shown in red and blue, respectively. (c) Pump-probe traces as a function of delay obtained by integrating the photocurrent over the area indicated by the red and blue boxes in panel (b). Thick gray lines are double-exponential fits to the data.

$$f(t) = \frac{a}{2}\left(1 + \mathrm{erf}\left(\frac{(t-t_0)\tau - \mathrm{FWHM}^2/(8\ln 2)}{\mathrm{FWHM}\,\tau/(2\sqrt{2\ln 2})}\right)\right)\exp\left(\frac{\mathrm{FWHM}^2/(8\ln 2) - 2(t-t_0)\tau}{2\tau^2}\right)$$

a is the amplitude of the pump-probe signal, FWHM is the full width at half maximum of the derivative of the rising edge, t_0 is the middle of the rising edge, erf is the error function, and τ is the exponential lifetime. This fitting function is obtained by convolving the product of a step function and an exponential decay with a Gaussian to account for the finite rise time of the signal.

The transient peak shifts in Fig. 3 in the main text were obtained as follows. In order to determine the position of the WS_2 valence band we extracted energy distribution curves (EDCs) at $k_{||} = 1.05\text{Å}^{-1}$ from Fig. S6a and fitted them with Gaussians (Fig. S6b). The transient position of the graphene π-band was obtained by fitting momentum distribution curves (MDCs)

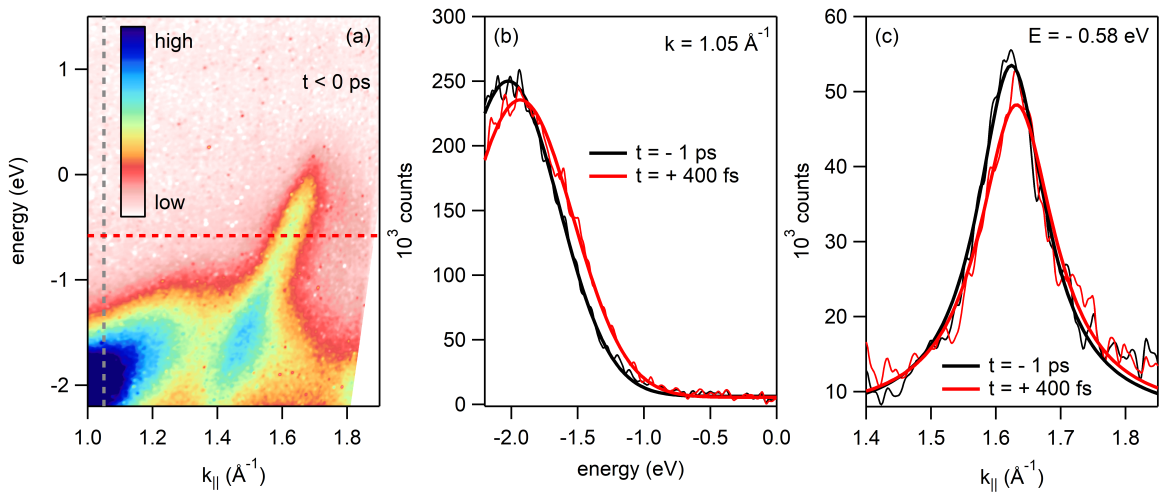

Figure S6: **Fits of transient peak position.** (a) Photocurrent along the ΓK-direction for negative pump-probe delay. (b) Energy distribution curves extracted along the dashed grey line in (a) together with Gaussian fits. (c) Momentum distribution curves extracted along the dashed red line in (a) together with Lorentzian fits.

at $E = -0.58$ eV from Fig. S6a with Lorentzians (Fig. S6c). The MDC position was then multiplied with the slope of the π-band $\hbar v_F$=7 eVÅ, yielding the transient band shift in Fig. 3b in the main text.

In order to determine the transient chemical potential and electronic temperature of the graphene π-band we proceed as follows. First we integrate the photocurrent over the area between the two dashed lines in Fig. S7a. Then we fit the resulting EDC with a Fermi-Dirac distribution in the vicinity of the equilibrium chemical potential for all pump-probe delays. These fits describe the transient electronic distribution well at all times, indicating a rapid thermalization of the photo-excited carriers in the π-band. The resulting shift of the chemical potential referenced with respect to the vacuum level $\mu_{e(vac)}$ and the transient electronic temperature T_e are shown in Figs. S8a and b, respectively. The transient shift of the chemical potential referenced with respect to the graphene Dirac point $\mu_{e(ED)}$ (Fig. S8c) is then calculated by subtracting the band shift in Fig. 2b of the main text from the shift of $\mu_{e(vac)}$ in Fig. S8a. From Figs. S8b and c

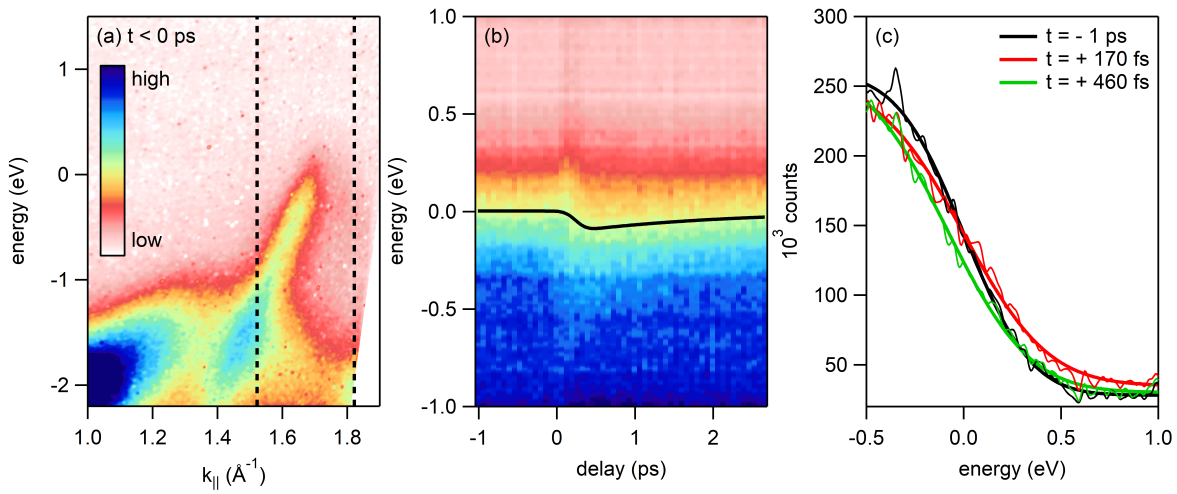

Figure S7: **Fermi-Dirac fits for graphene π-band.** (a) Photocurrent along the ΓK-direction for negative pump-probe delay. (b) Photocurrent integrated over the area between the two dashed lines in (a) as a function of pump-probe delay. The black line indicates the transient position of the chemical potential referenced to the vacuum level $\mu_{e(vac)}$. (c) Momentum-integrated energy distribution curves from (b) for three different time delays together with Fermi-Dirac fits.

we can then directly calculate the change of the total number of electrons in the graphene layer (Fig. S8d) via

$$\Delta n_e(t) = \int_{-\infty}^{\infty} dE\, \rho(E)\, [f_{FD}(E, \mu(t), T(t)) - f_{FD}(E, \mu_0, T_0)]$$

where $\rho(E) = \frac{2A_c}{\pi} \frac{|E-ED|}{\hbar^2 v_F^2}$ is the density of states with the unit cell are $A_c = \frac{3\sqrt{3}a^2}{2}$ and the lattice constant $a = 1.42\,\text{Å}$. The equilibrium chemical potential $\mu_0 = -0.3\,\text{eV}$ was obtained from the high-resolution photoemission spectrum in Fig. 1a of the main text. The transient chemical potential is given by $\mu(t) = \mu_0 + \Delta\mu_{e(ED)}(t)$. The equilibrium temperature is $T_0 = T(t < 0\,\text{ps}) = 300\,\text{K}$. The number of transferred holes shown in Fig. 4 of the main text is then given by $\Delta n_h(t) = -\Delta n_e(t)$.

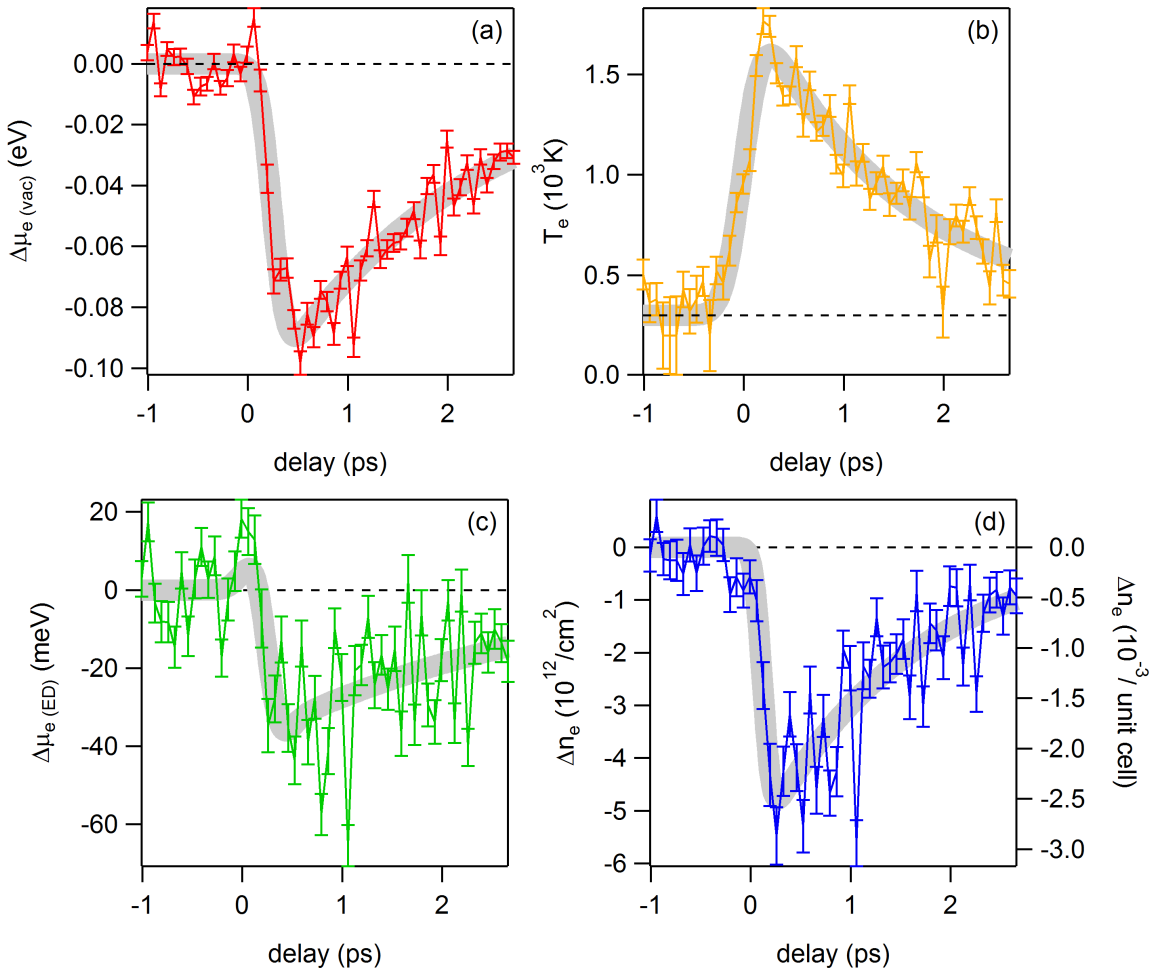

Figure S8: **Result of Fermi-Dirac fits for graphene π-band.** (a) Change of the chemical potential referenced to the vacuum level $\mu_{e(vac)}$ as a function of pump-probe delay. (b) Electronic temperature as a function of pump-probe delay. Thick lines in (a) and (b) are exponential fits with lifetimes of 2.0 ± 0.2 ps and 1.5 ± 0.1 ps, respectively. (c) Shift of the chemical potential referenced to the Dirac point $\mu_{e(ED)}$ obtained by subtracting the π-band shift from Fig. 2b from the main text from $\mu_{e(vac)}$ in panel (a). (d) Change of the number of electrons in the π-band as a function of pump-probe delay together with an exponential fit yielding a lifetime of 1.5 ± 0.2 ps.

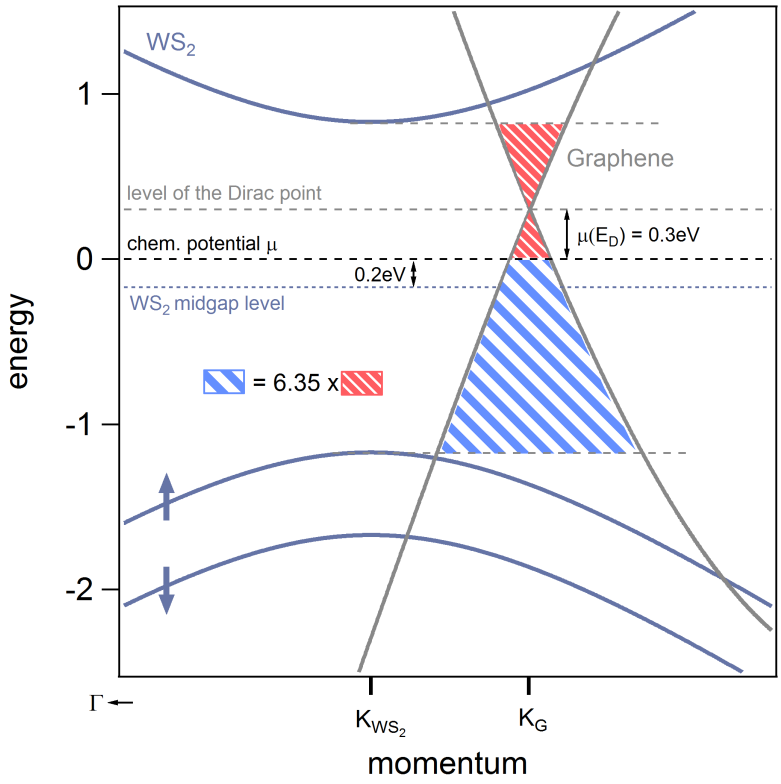

Figure S9: **Scattering phase space.** The WS_2 and graphene band structures are shown in blue and gray, respectively. The number of available electronic final states for electron and hole transfer are illustrated by red and blue areas, respectively.

Section S4. Phase space for electron and hole transfer

In Fig. S9 we illustrate the number of available electronic final states for electron and hole transfer, respectively. The available number of final states (NOFS) for electrons and holes is given by

$$\text{NOFS}_e = \int_{-\infty}^{E_{CB}} dE\, \rho(E)(1 - f_{FD}(E, \mu, T))$$
$$\text{NOFS}_h = \int_{E_{VB}}^{\infty} dE\, \rho(E) f_{FD}(E, \mu, T)$$

where E_{CB} (E_{VB}) is the position of the conduction band minimum (valence band maximum) of WS_2. The density of states $\rho(E)$ of graphene depends on the position of the Dirac point. The Fermi-Dirac distribution $f_{FD}(E, \mu, T)$ accounts for Pauli blocking. In the present case of the WS_2/graphene heterostructure the blue area (available electronic final states for hole transfer) is ~ 6 times bigger than the red area (available electronic final states for electron transfer) which we expect to directly affect the corresponding charge transfer rates.

We would like to stress that a proper calculation of the scattering phase space requires detailed knowledge about the scattering mechanism (e.g. electron-electron or electron-phonon scattering) and should also include the phase space for the corresponding scattering partner.

Section S5. Charge transfer exciton versus free electron-hole pairs

In order to assess the stability of a putative interlayer exciton one needs to compare the exciton binding energy to the thermal energy of the carriers. Fermi-Dirac fits of the graphene π-band yield peak carrier temperatures of 1500 K (see Fig. S8b). At this temperature only excitons with binding energies in excess of $k_B T = 130$ meV are expected to be stable. Neither the existence nor the binding energy of a putative interlayer exciton in WS_2/graphene is discussed in literature. We speculate that — provided that the interlayer exciton exists — its binding energy

is most likely smaller than the binding energy of the A-exciton in monolayer WS_2 (which is 320 meV (19)) due to enhanced screening by the metallic graphene layer.

Further, as shown in Fig. S1 our samples consist of triangular WS_2 islands on top of the graphene layer with a total coverage of 40% and a spacing between WS_2 islands of $1 - 10\,\mu$m. Due to the extreme surface sensitivity of ARPES we are only able to probe the graphene layer in the areas where it is uncovered. Also, the tr-ARPES measurements average over the area of the XUV spot with a diameter of $\sim 300\,\mu$m. From the fact that the pump-probe signal of the graphene π-band of our WS_2/graphene heterostructure (main text) is clearly different from the one of pure graphene (Fig. S5) we conclude that all or a significant part of the holes that are transferred from WS_2 to graphene are rapidly delocalized over the complete graphene layer. These points seem to be in favor of free electron-hole pairs rather than charge transfer excitons.